

Gamma-ray observation towards the young massive star cluster NGC 6618 in the M17 region

Bing Liu,^{1,2,3} Rui-zhi Yang,^{1,2,3}★ Zhiwei Chen⁴

¹Department of Astronomy, School of Physical Sciences, University of Science and Technology of China, Hefei, Anhui 230026, China

²CAS Key Laboratory for Research in Galaxies and Cosmology, University of Science and Technology of China, Hefei, Anhui 230026, China

³School of Astronomy and Space Science, University of Science and Technology of China, Hefei, Anhui 230026, China

⁴Purple Mountain Observatory, Chinese Academy of Sciences, Yuanhua Road 10, 210023 Nanjing, China

Accepted XXX. Received YYY; in original form ZZZ

ABSTRACT

Young massive clusters have been established as a new population of gamma-ray sources and potential cosmic ray (CR) accelerators. In this paper, we report the detection of gamma-ray emissions near the young star cluster NGC 6618, which is one of the youngest star clusters in our Galaxy. The detected gamma-ray emissions can be divided into two components. One component is point-like and reveals harder spectrum, while the other is extended and with softer spectrum. Such spectral features are significantly different from other young massive clusters and may be due to the propagation effects of CRs accelerated in NGC 6618.

Key words: cosmic rays – gamma-rays: ISM – open clusters and associations: individual: M17 (NGC 6618)

1 INTRODUCTION

Young massive star clusters (YMCs) are established as a new population of gamma-ray sources in recent years and are believed to be able to account for the acceleration of a significant part of Galactic cosmic rays (CRs) (Aharonian et al. 2019). Several such systems are detected in GeV or TeV gamma-ray band, with significant spatial extensions up to more than 50 pc and a universal hard gamma-ray spectrum which can be described by a powerlaw function with an index of 2.2 – 2.4. More interestingly, the derived CR spatial distribution reveals a $\frac{1}{r}$ profile, which is consistent with a continuous injection of CRs. Considering the size of the source, the CRs are believed to be injected in the time scale of $\gtrsim 10^5$ years, which is longer than the acceleration phase of supernova remnants (SNRs). Moreover, the massive star winds, which can be as high as $\gtrsim 3000 \text{ km s}^{-1}$ in O-type stars and Wolf-Rayet stars, are powerful enough to accelerate CRs to high energies nearly in the whole lifetime of the massive stars (Cesarsky & Montmerle 1983). In this regard, the CRs in YMCs are more likely accelerated by "live" stars rather than the "dead" stars. In an observational point of view, several YMCs have been detected in gamma-rays, such as Cygnus Cocoon (Ackermann et al. 2011), NGC 3603 (Yang & Aharonian 2017; Saha et al. 2020), Westerlund 1 (Abramowski et al. 2012), Westerlund 2 (Yang et al. 2018), RSGC 1 (Katsuta et al. 2017; Sun et al. 2020a), W40 (Sun et al. 2020b) and W43 (Yang & Wang 2020).

The YMC NGC 6618, with an age less than 3 Myr (Jiang et al. 2002), is one of the youngest massive star clusters in our Galaxy,

and contains hundreds of stars earlier than B9 including dozens of O stars (Chini et al. 1980; Hoffmeister et al. 2008). The OB stars in the cluster, especially the most massive ones such as the O4 binary system (CEN 1a + CEN 1b; Hoffmeister et al. 2008), provide the ionizing power for the H II region, M17 nebula (also known as Omega Nebula or W38), which is located in the Sagittarius spiral arm (Elmegreen et al. 1979; Reid et al. 2019) at a distance $\approx 2.0 \text{ kpc}$ (Xu et al. 2011; Chibueze et al. 2016). Moreover, the cluster is also thought to be the source of energetic feedback to the dense molecular clouds (MCs) surrounding M17 nebula (Nguyen-Luong et al. 2020).

The MC associated with M17 was first detected in CO molecular line emission at velocity around 20 km s^{-1} , and the line emission extends along the Galactic plane for at least 85 pc and has a total mass in the order of $10^6 M_{\odot}$ (Elmegreen & Lada 1976), comparable to the typical definition of the giant MC (GMC). The M17 GMC is usually split into three regions according to the relative location with respect to NGC 6618. The cloud in the north, i.e., M17 North cloud, has the smallest mass and size (Wilson et al. 2003). The adjacent cloud in the southwest, i.e., M17 SW cloud, is the densest region and highly clumpy (Stutzki & Guesten 1990; Nguyen-Luong et al. 2020), and contributes most of the forming stars of low- to high-mass (Povich et al. 2009; Chen et al. 2012, 2013, 2015, 2021; Ramírez-Tannus et al. 2017; Lim et al. 2020). The cloud extending to the very southwest, i.e., M17 SWex, appears as an infrared dark cloud and hosts sites of low- to intermediate-mass star formation (Povich & Whitney 2010; Povich et al. 2016; Yin et al. 2022). By comparing the dense gas properties of M17 SW and M17 SWex, Nguyen-Luong et al. (2020) found that the clumps in M17 SW are

★ E-mail: yangrz@ustc.edu.cn

denser, more compact, and more gravitationally bound than those in M17 SWex.

If the massive stars in NGC 6618 can accelerate protons to very high energies, then these protons could illuminate the clouds around them via proton-proton inelastic collisions. Recently released *Fermi*-LAT 10-year Source Catalog (4FGL-DR2, Ballet et al. 2020) revealed a gamma-ray point source that located in the direction of M17 region (named as 4FGL J1820.4-1609c), which is possibly associated with NGC 6618. In such a complex region as described above, the origin of these gamma-rays is still an intriguing puzzle and requires a careful and comprehensive investigation. In the following section, we present the details of the analysis of *Fermi*-LAT data and the results. Then in Sect. 3, we investigate the gas distributions around M17. Next in Sect. 4, we combine the multiwavelength observations with gamma-ray results to explore the radiation mechanism of the gamma-rays. Finally, we summarise the main conclusions and implications of our study in Sect. 5.

2 FERMI-LAT DATA ANALYSIS AND RESULTS

To study the gamma-ray emission in M17 region, we collected about 12.5 years (from 2008-08-04 15:43:36 (UTC) to 2021-04-16 23:02:55 (UTC)) of *Fermi*-LAT Pass 8 data, and used Fermi-tools from Conda distribution¹ and applied the latest version of the instrument response functions *P8R3_SOURCE_V3*. Given the energy-dependent point-spread function (PSF) of the LAT data, we used different datasets to optimize the spatial and spectral analyses. The region of interest (ROI), centered at M17 (R.A. = 275.195°, Dec. = −16.172°, J2000) is adjusted for each dataset correspondingly. The source models, generated by *make4FGLxml.py*², consist of the sources in 4FGL-DR2 within the ROI enlarged by 10°, the Galactic diffuse background emission (*gll_iem_v07.fits*), and isotropic emission (*iso_P8R3_SOURCE_V3_v1.txt*).

2.1 Spatial analysis and results

In order to study possible energy dependent morphology in M17 region, we conduct separate spatial analyses for gamma-rays within different energy ranges, including 0.5–5 GeV, 5–500 GeV, and 0.5–500 GeV, hereinafter referred as LE, HE and ALL datasets, respectively. Specific parameters of the cuts and details of each dataset are provided in Table. 1.

Following procedures were applied to the LE and HE datasets respectively, in which the spectral type of the tested sources are all set to be simple PowerLaw (PL). At first, we used *gtlike* to optimize the source models. Since 4FGL J1820.4-1609c is very likely associated with NGC 6618 and cannot be treated as background. Thus we removed 4FGL J1820.4-1609c from the optimized background source models, and generated the residual test statistic (TS) maps. As shown in Fig. 1, the residual gamma-rays of LE dataset are very diffusive and shifted to the west of M17, meanwhile, the gamma-rays of HE dataset are rather point-like and in the direction of NGC 6618. Therefore, to find out whether the residual emission is extended or not, we added a point-like source or an extended source (using RadialGaussian model) to the modified source model, from which 4FGL J1820.4-1609c are deleted. The added point or the center of the gaussian disk is set at the peak position of the residual

TS map for each dataset, which is presented in Table 2. The radius (σ_{disk}) of the disk varies from 0.1° to 0.5° with a step of 0.05°. Then we fitted above modified models to calculate the corresponding TS_{ext} , defined as $-2 \log(\mathcal{L}_{\text{p}}/\mathcal{L}_{\text{ext}})$. The \mathcal{L}_{p} is the maximum likelihood of the model with a point source added at the peak position, and the \mathcal{L}_{ext} is the acquired maximum likelihood of the tested gaussian disk models. For LE dataset, the maximum TS_{ext} (290.6) is obtained when $\sigma_{\text{disk}} = 0.35^\circ$, meaning the significance of the extension is about 17.0. However, for HE dataset, gaussian disk models show no improvement compared to the point source assumption. The specific results for the spatial analyses of LE and HE datasets are listed in Table 2.

Finally, we analysed ALL dataset in order to test whether one source with the spatial model obtained from LE or HE dataset (1-source hypothesis) or two sources with the spatial models acquired from both LE and HE datasets (2-source hypothesis) could represents the overall data better. By comparing the maximum $\log(\text{likelihood})$ of these models, we obtained the significance of 2-source hypothesis versus 1-source hypotheses or the non-modified 4FGL-DR2 model is $\sim 9\sigma$.

2.2 Spectral analysis and results

From above analysis, we noticed that the morphology of gamma-ray emission around M17 region is energy-dependent and these gamma-rays are better represented as two separate components. In the following spectral analysis applied to ALL dataset, we replace 4FGL J1820.4-1609c with two sources: one source is an extended source with $\sigma_{\text{disk}} = 0.35^\circ$ lying to the west of NGC 6618 (hereafter referred as Src A), and the other is a point-like source that is coincided with NGC 6618 (hereafter referred as Src B).

To find out the spectral shape of Src A and Src B, we performed likelihood-ratio test for spectral models including Log-Parabola (LogP), PLSuperExpCutoff2 (PLEC), BrokenPowerLaw (BPL), in which the PL model is the null hypothesis. The formulae and free parameters of these spectral model are presented in Table. 3. The significance of the tested model σ_{model} is defined as $\sqrt{-2 \log(\mathcal{L}_{\text{PL}}/\mathcal{L}_{\text{model}})}$. Firstly, we changed the spectral type of Src A from PL to LogP, PLEC and BKL respectively, keeping the spectral model of Src B to be PL. Next, we set the spectral model of Src A to be PL, and change the spectral type of Src B from PL to LogP, PLEC, and BPL, respectively. As shown in Table. 4, those more complicated spectral models do not improve the overall fitting results ($\sigma_{\text{model}} < 3$), and the simple PL model is capable to represent their spectral shape. The best-fit results of the PL model for Src A and Src B are listed in Table. 5.

The spectral energy distributions (SEDs) of Src A and Src B as shown in Fig. 2 were extracted from the maximum likelihood analysis of source class events in nine logarithmically spaced energy bins within 0.5–500 GeV. Expect the energy range of the selected events, other parameters applied for the data preparation are the same as the ALL datasets. During the fitting process, the free parameters only include the normalization parameters of the sources with the significance $\geq 5\sigma$ within 10° from ROI center as well as the Galactic and isotropic diffuse background components, while all the other parameters are fixed to their best-fit values from above analysis of ALL dataset in which the spectral shape of Src A and Src B are assumed to be PL. In addition to the uncertainties caused by the statistics and the effective area (green error bars in Fig. 2), we also estimated the uncertainties caused by the imperfection model of the Galactic diffuse background (blue error bars in Fig. 2) by artificially varying its normalization by $\pm 6\%$ from the best-fit value of each

¹ <https://github.com/fermi-lat/Fermitools-conda/>

² <https://fermi.gsfc.nasa.gov/ssc/data/analysis/user/make4FGLxml.py>

Table 1. Description of the datasets for spatial analysis

| Name | ALL | LE | HE |
|-------------------------------------|----------------------------|----------------------------|----------------------------|
| E_{min} (GeV) | 0.5 | 0.5 | 5 |
| E_{max} (GeV) | 500 | 5 | 500 |
| ROI | $20^\circ \times 20^\circ$ | $20^\circ \times 20^\circ$ | $10^\circ \times 10^\circ$ |
| z_{max} | 90° | 90° | 105° |
| evclass | 128 | 128 | 128 |
| evtype | 16/32 | 32 | 16 |
| N_{ebins} | 30 | 10 | 16 |
| DATA_QUAL | > 0 | > 0 | > 0 |
| LAT_CONFIG | 1 | 1 | 1 |
| free ^a /all ^b | $10^\circ / 25^\circ$ | $10^\circ / 25^\circ$ | $5^\circ / 15^\circ$ |

^a The radius in degrees from the center of ROI within which the spectral parameters are free to change for sources with significance > 5.

^b The radius in degrees from the center of ROI within which sources are included in the XML file.

Table 2. Spatial analysis results of the LE and HE datasets

| Name | LE | HE |
|---------------------|--------------------|---------------------|
| Position (Ra, Dec) | (274.65°, -16.30°) | (275.120°, -16.20°) |
| \mathcal{L}_0 | 645931.3 | -36584.1 |
| \mathcal{L}_p | 646128.2 | -36579.1 |
| \mathcal{L}_{ext} | 646273.5 | -36578.8 |
| σ_{disk} (°) | 0.35 ± 0.05 | 0.10 ± 0.05 |
| TS _{ext} | 290.6 | 0.3 |

The position refers to the peak location of the residual TS map for each dataset. σ_{disk} is the radius of gaussian disk of the maximum -log(likelihood) among the extension test models in which σ_{disk} varies from 0.1° to 0.5° with a step of 0.05° and the center of the disk located at the corresponding peak position. The \mathcal{L}_0 is the likelihood of the non-modified 4FGL-DR2 model. The \mathcal{L}_p is the likelihood of the model with 4FGL J1820.4-1609c removed and a point source added at the peak position. The \mathcal{L}_{ext} is the -log(likelihood) of best-fit gaussian disk model. TS_{ext} = $-2 \log(\mathcal{L}_p / \mathcal{L}_{ext})$.

Table 3. Formulae for gamma-ray spectral analysis

| Name | Formula | Free parameters |
|------|--|--------------------------------|
| PL | $\frac{dN}{dE} = N_0 \left(\frac{E}{E_0} \right)^{-\Gamma}$ | N_0, Γ |
| LogP | $\frac{dN}{dE} = N_0 \left(\frac{E}{E_b} \right)^{-\Gamma - \beta \log\left(\frac{E}{E_b}\right)}$ | N_0, Γ, β |
| PLEC | $\frac{dN}{dE} = N_0 \left(\frac{E}{E_0} \right)^{-\Gamma_1} \exp\left(-\left(\frac{E}{E_{cut}}\right)^b\right)$ | N_0, Γ, E_{cut}, b |
| BPL | $\frac{dN}{dE} = \begin{cases} N_0 \left(\frac{E}{E_b} \right)^{-\Gamma_1} & : E < E_b \\ N_0 \left(\frac{E}{E_b} \right)^{-\Gamma_2} & : E > E_b \end{cases}$ | $N_0, \Gamma_1, \Gamma_2, E_b$ |

energy bin and recording flux deviation of the source due to above changes as the systematic error, following the method from [Abdo et al. \(2009\)](#). We note that in lower energy range (0.5–1 GeV, first bin of the SEDs), the fluxes of both Src A and Src B drop dramatically when the Galactic diffuse background was artificially enhanced.

3 GAS DISTRIBUTIONS NEAR M17

In this work, we analysed the large scale $^{12}\text{CO}/^{13}\text{CO}$ ($J=1-0$) molecular line data toward the M17 GMC, as a part of the Milky Way Imaging Scroll Painting (MWISP) project. The details of MWISP

Table 4. The significance of the tested spectral models (σ_{model}) for Src A and Src B

| Spectral Model | LogP | PLEC | BPL |
|--------------------|------|------|-----|
| Src A ^a | 2.3 | 2.3 | 2.2 |
| Src B ^b | 2.5 | 2.3 | 2.3 |

^a The spectral type of Src B is PL

^b The spectral type of Src A is PL

Table 5. The best-fit results of the PL model for Src A and Src B

| | Γ | Flux ($\text{ph cm}^{-2} \text{s}^{-1}$) | Luminosity ^a (erg s^{-1}) | significance ^b σ |
|-------|-----------------|---|--|---------------------------------------|
| Src A | 2.73 ± 0.08 | 1.58×10^{-8} | 1.14×10^{33} | 15 |
| Src B | 2.41 ± 0.06 | 5.67×10^{-9} | 5.67×10^{32} | 12 |

^a The distance of Src A and Src B is assumed to be 2 kpc.

^b The significance of each source $\approx \sqrt{\text{TS}}$.

project are referred to [Su et al. \(2019\)](#). The $^{12}\text{CO}/^{13}\text{CO}$ ($J=1-0$) molecular data used in this work span from the galactic longitude 13° to 16° and the galactic latitude -1.5° to 0.5° . After fitting the baseline and calibrating the main beam efficiency, the reduced 3D data cubes with a grid spacing of $30''$ have a typical root mean square noise level of ~ 0.5 K for ^{12}CO ($J=1-0$) transition line and ~ 0.3 K for ^{13}CO ($J=1-0$) transition line at a channel width of 0.16 km s^{-1} . The spatial resolution of the CO data is $\sim 50''$.

The large-scale ^{12}CO and ^{13}CO gas distributions over the area from the galactic longitude $13^\circ 67'$ to $15^\circ 39'$ and the galactic latitude $-0^\circ 87'$ to $-0^\circ 27'$ were studied earlier in [Nguyen-Luong et al. \(2020\)](#); however, the spatial extent of Src A is not fully covered by this research. The bulk of the M17 GMC emission is seen in the velocity range $10\text{--}30 \text{ km s}^{-1}$ from the Sagittarius arm, while the components at $\sim 37\text{--}38 \text{ km s}^{-1}$ and $\sim 57 \text{ km s}^{-1}$ are from the spiral arms at larger distances ([Zhan et al. 2016](#); [Nguyen-Luong et al. 2020](#)). Therefore, we only considered the emission around $10\text{--}30 \text{ km s}^{-1}$ for the MWISP CO data.

As shown in Fig. 3, Src B is much closer to the M17 SW cloud (hereafter referred to as cloud B) than to the M17 north cloud. Cloud B shows a peak intensity at the velocity $V_{\text{LSR}} \approx 20 \text{ km s}^{-1}$, and a velocity range from 10 to 28 km s^{-1} (see Fig. 4). At velocity greater than 28 km s^{-1} , the CO ($J=1-0$) line emission shows an extended distribution at a level of $T_{\text{MB}} \sim 2\text{--}3$ K. The molecular gas within the region of Src A (hereafter referred to as cloud A, the white circle in Fig. 3) shows velocity in the range from 10 to 34 km s^{-1} , much broader than the velocity range of cloud B (see Fig. 4). For cloud A, the peak intensity of the ^{13}CO ($J=1-0$) line emission is at $V_{\text{LSR}} \approx 27 \text{ km s}^{-1}$. However, both cloud B and M17 SWex cloud show peak intensity at $V_{\text{LSR}} \approx 20 \text{ km s}^{-1}$. The large difference in V_{LSR} , together with the far distance from Src A to cloud B and M17 SWex cloud, indicate that Src A is not associated with the molecular gas at the velocity $V_{\text{LSR}} \approx 20 \text{ km s}^{-1}$. Thus, we suggest that Src A is associated with cloud A with a peak intensity at $V_{\text{LSR}} \approx 27 \text{ km s}^{-1}$.

The bulk masses of clouds A and B depend strongly on the adopted velocity range of the ^{12}CO line emission. For cloud B that possibly associated with Src B, a velocity range $13\text{--}25 \text{ km s}^{-1}$ is assumed for the ^{12}CO line emission. A wider range in velocity would definitely include more molecular gas. The molecular gas mass estimated from the velocity range $13\text{--}25 \text{ km s}^{-1}$ represents

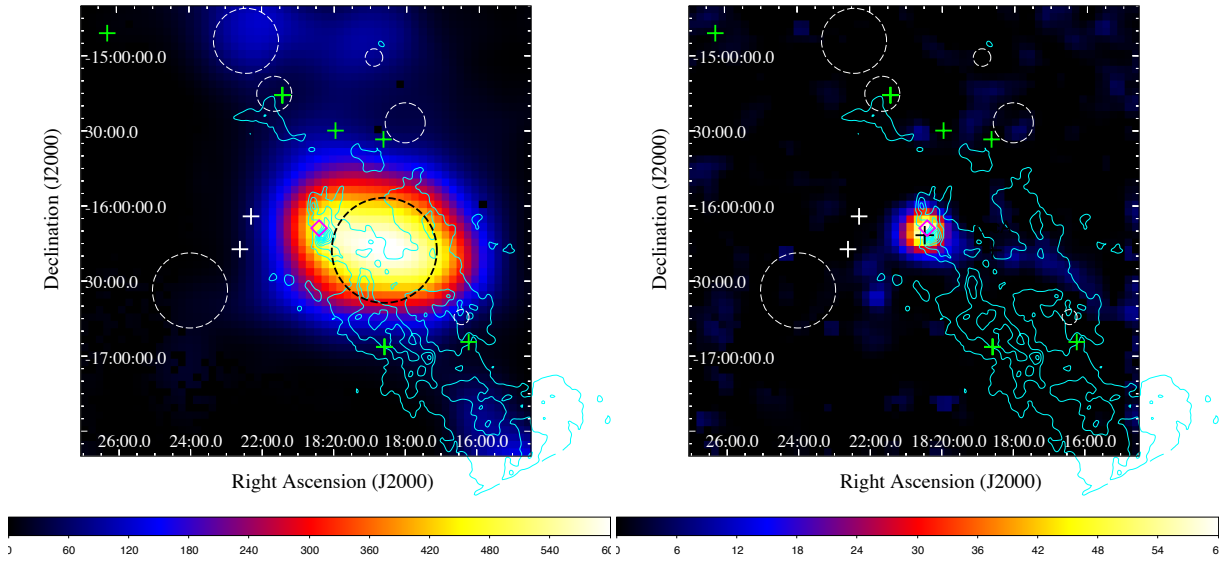


Figure 1. Smoothed residual TS maps centered at M17 for LE dataset (left) and HE dataset (right), respectively. The green crosses show the position of nearby sources listed in 4FGL-DR2, and the magenta diamond represents 4FGL J1820.4-1609c, which is removed from the fitted background model. The white dashed circle and crosses illustrate the nearby supernova remnants and pulsars, respectively. The black dashed circle illustrates the best-fit gaussian disk model (Src A) from fitting LE dataset, and the black cross represents the position of the point source (Src B) for fitting HE dataset. The maps are overlaid with contours generated from ^{13}CO ($J=1-0$) integrated intensity map in the velocity range $10\text{--}34\text{ km s}^{-1}$ at ten linear scale levels between 15 and 150 K km s^{-1} . See Sect. 2.1 for details.

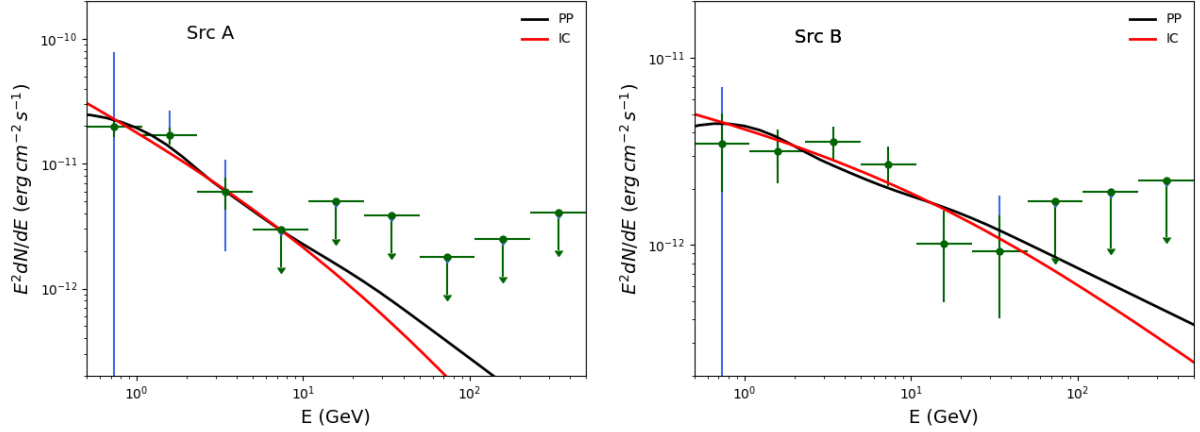


Figure 2. SEDs of Src A (left) and Src B (right) respectively. For each data point, the green error bar indicates the uncertainty caused by the statistics and the effective area, and the blue error bar shows the uncertainty caused by the imperfection model of the Galactic diffuse background. The best-fit PP models (black lines) and IC models (red lines) for Src A and Src B are represented. See Sect. 2.2 and Sect. 4 for details.

the lower limit of the mass of cloud B. We see from Figure 4 that the ^{12}CO line spectrum averaged over Src A shows line width of 18 km s^{-1} and equal contributions from clouds A and B. Since it is impossible for us to confirm an exact range in velocity for cloud A that is likely related to Src A, here we adopt a velocity range $25\text{--}34\text{ km s}^{-1}$ for cloud A. This velocity range would miss a fraction of molecular gas with velocity exceeding this range, but preclude mostly the molecular gas at velocity about 40 km s^{-1} from the Scutum arm. Therefore, the integrated intensity of ^{12}CO line emission (W_{CO}) over the ranges $25\text{--}34\text{ km s}^{-1}$ and $13\text{--}25\text{ km s}^{-1}$ are obtained for clouds A and B, respectively.

Next, we used the nominal X -factor, $2 \times 10^{20}\text{ cm}^{-2}/(\text{K km s}^{-1})$,

for the conversion from W_{CO} to the molecular hydrogen column density $N(\text{H}_2)$. For cloud A, ^{13}CO line emission shows a prominent cavity of little emission toward the center of cloud A, while ^{12}CO line emission toward the same cavity is still significant. Thus, for cloud A, the average $N(\text{H}_2)$ estimated from the ^{13}CO line emission (hereafter referred as $N(\text{H}_2)_{^{13}\text{CO}}$) is $8.1 \times 10^{21}\text{ cm}^{-2}$, slightly lower than the average $N(\text{H}_2)$ estimated from ^{12}CO line emission ($N(\text{H}_2)_{^{12}\text{CO}}$), which is $1.0 \times 10^{22}\text{ cm}^{-2}$. As for cloud B, the $N(\text{H}_2)_{^{12}\text{CO}}$ is $4.9 \times 10^{22}\text{ cm}^{-2}$, which should be severely underestimated because the ^{12}CO line emission is optically thick.

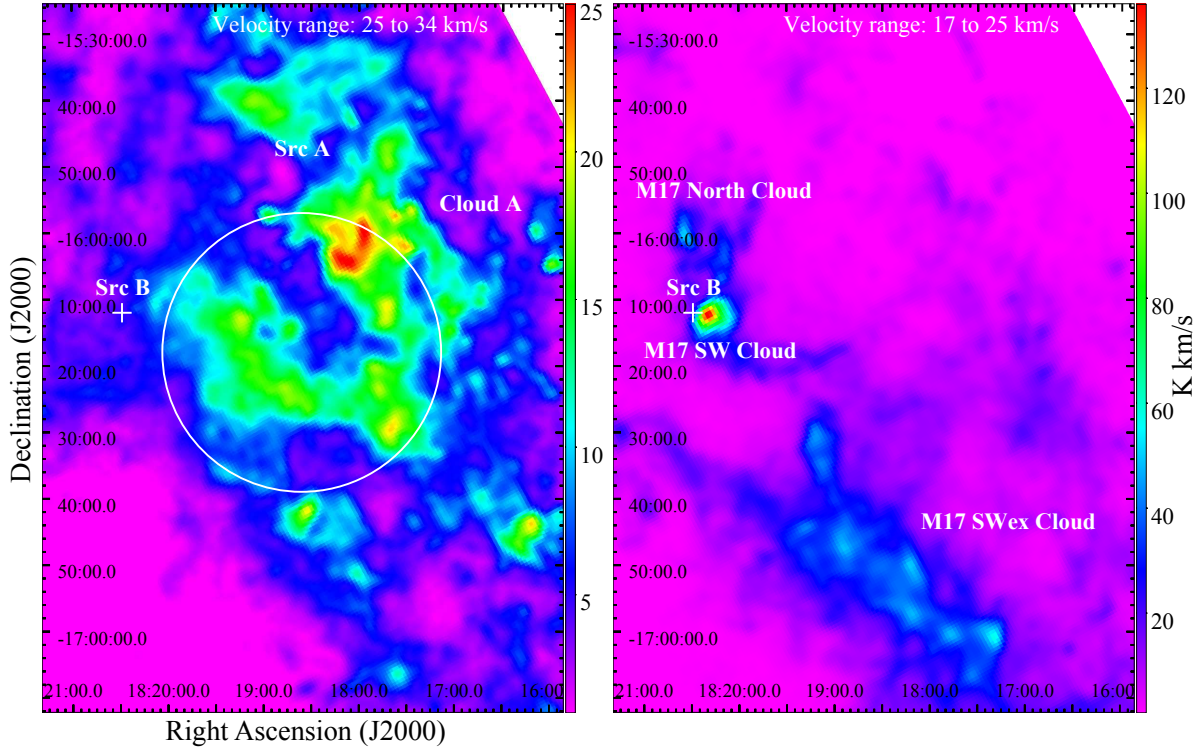


Figure 3. The integrated intensity map of ^{13}CO ($J=1-0$) line emission in the velocity range 25–33 km s^{-1} (left) and 17–25 km s^{-1} (right) respectively. The white circle represents the extended gamma-ray component (Src A), and the white cross shows the location of point-like component (Src B). See Sect. 3 for details.

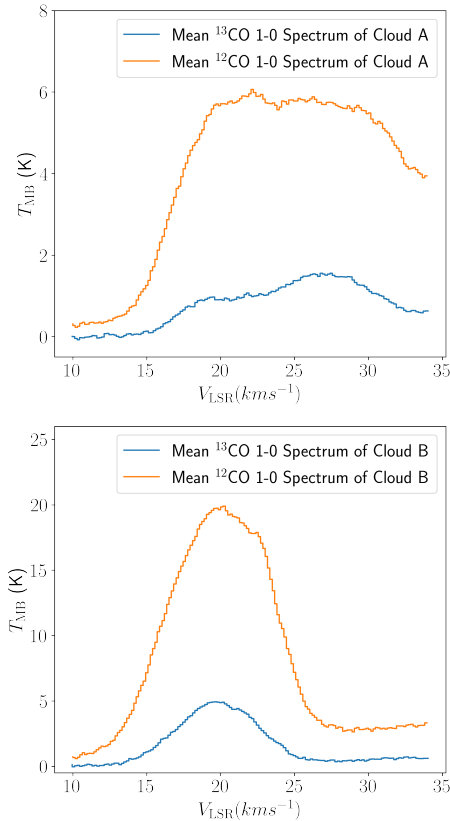


Figure 4. Mean CO spectra for molecular gases (clouds A and B) that are possibly associated with Src A (top) and Src B (bottom).

In comparison, the estimated $N(\text{H}_2)_{^{13}\text{CO}}$ of cloud B can reach to $3.4 \times 10^{23} \text{ cm}^{-2}$ ³.

Assuming a distance of 2.0 kpc, the radius of cloud B is ~ 2.5 pc. Thus, the total gas mass of cloud B is $2.2 \times 10^4 M_\odot$ according to its $N(\text{H}_2)_{^{12}\text{CO}}$ or $1.5 \times 10^5 M_\odot$ according to its $N(\text{H}_2)_{^{13}\text{CO}}$. Nguyen-Luong et al. (2020) estimated a total gas mass of $1.43 \times 10^5 M_\odot$ for the molecular gas near to the YMC NGC 6618, including cloud B and the less massive M17 North cloud. Therefore, we adopt a total gas mass of $1.5 \times 10^5 M_\odot$. Then the corresponding hydrogen number density $n(\text{H})$ of cloud B is $4.4 \times 10^4 \text{ cm}^{-3}$, assuming a thickness of 5 pc. Similarly, the total gas mass of cloud A is about $1.3 \times 10^5 M_\odot$, comparable to that of cloud B. Assuming a thickness of 5 pc for cloud A, a value as the same as cloud B, the hydrogen number density $n(\text{H})$ of cloud A is estimated to be $1.3 \times 10^3 \text{ cm}^{-3}$. However, if the thickness of cloud A is comparable to the projected size of the plane of sky, i.e., be as large as 25 pc, it will yield a lower density, $\sim 2.6 \times 10^2 \text{ cm}^{-3}$. Thus, we suggest that $n(\text{H})$ of cloud A is likely between $\sim 2.6 \times 10^2 \text{ cm}^{-3}$ and $\sim 1.3 \times 10^3 \text{ cm}^{-3}$.

In short, the molecular gas components possibly associated with Src A and Src B, clouds A and B, are very different in density, size, and kinematics. At a $V_{\text{LSR}} \sim 27 \text{ km s}^{-1}$, cloud A is a very extended molecular cloud of moderate density. Cloud B is a compact dense molecular cloud with a $V_{\text{LSR}} \sim 20 \text{ km s}^{-1}$.

³ This method makes use of both ^{12}CO and ^{13}CO line emissions and assumes the local thermal equilibrium state for the two molecules. Detailed description of this method is referred to Chen et al. (2022) and references therein.

4 DISCUSSION

To investigate the possible radiation mechanisms of the gamma-rays in M17 region, we fit the SEDs of Src A and Src B with both leptonic scenario, i.e., the inverse Compton scattering (hereafter referred as IC model) and hadronic scenario, i.e., proton-proton inelastic collision (hereafter referred as PP model). The fitting was performed using Naima package⁴ (Zabalza 2015), which includes tools to perform Markov Chain Monte Carlo (MCMC) fitting of nonthermal radiative processes to the data and allows us to implement different functions. Here the distribution function of the parent particles was assumed to be simple power law. The best-fit results are illustrated in Fig. 2, in which the black lines are the results of PP model fitting and the red lines are results of IC model fitting. The corresponding parameters are listed in Table 6.

Around M17 region, there are several known pulsars and SNRs (see Fig. 1), but none of them overlaps with Src A or Src B. Although we cannot formally rule out the possibility that the emissions are related with some unknown pulsars or SNRs, the extension of Src A and the hard spectrum of Src B can exclude the possibilities that those sources are pulsars. However, the pulsar wind nebula related with the unknown pulsars can be a possible explanation. In addition, considering the spatial correlation of both Src A and Src B with dense gas, it is possible that the CRs escaped from SNRs in the vicinity interacting with dense gas produced the detected gamma-rays.

Another scenario is associating Src A and Src B with the YMC NGC 6618. NGC 6618 contains more than 40 OB stars (Hoffmeister et al. 2008), the total wind power of these stars can be estimated using the estimations in Domingo-Santamaría & Torres (2006), which amounts to more than $5 \times 10^{37} \text{ erg s}^{-1}$. Taking into account the age of 500 kyr, the total energy injected by NGC 6618 is about 10^{51} erg , which is comparable to a typical supernova explosion. Thus, this system is powerful enough to accelerate enough CRs to account for the detected gamma-ray emissions. Furthermore, the hard spectrum of Src B is also similar to other YMC systems. The soft spectrum of Src A is unique compared with other YMCs. Generally speaking, if we assume the CRs are injected continuously by the YMC, the CR energy spectrum in the vicinity can be expressed as $F(E) \sim \frac{Q(E)}{D(E)}$, where $Q(E)$ and $D(E)$ is the injection spectrum and diffusion coefficient, respectively (Aharonian & Atoyan 1996). Therefore, a natural explanation for the different spectral indices of Src A and Src B is a different $D(E)$ in the corresponding regions. Indeed, due to the higher density and stronger magnetic field inside the YMCs, the environment can be significantly different from the interstellar medium (ISM) in the Galaxy. The MHD turbulent cascade in the ISM can be damped out effectively and CRs will stream along field lines and transport via a process of field line random walk. Such process have been studied in detail in starburst galaxies in Krumholz et al. (2020), and the environments in YMCs are comparable to these starburst galaxies. In this case, the effective diffusion coefficient is energy independent at lower energy (below some critical energy E_{br}), thus the propagated CR spectra are the same as the injected spectra. This provide an natural explanation for hard spectrum in Src B and in other YMC systems. If we assume a continuous injection, the CR energy density scales as $\frac{1}{r}$, where r is the distance to the CR source. Thus, the CR density can be much smaller in Src A than in Src B, if we assume the CRs are injected from NGC 6618. For Src A, the CR transport may be still dominated by the CR scattering

Table 6. SED fit results for different radiation models of Src A and Src B

| | Model | Index | W_p or W_e (erg) ^a |
|-------|-------|------------------------|---------------------------------------|
| Src A | PP | $3.13^{+0.14}_{-0.12}$ | $4.67^{+0.21}_{-0.18} \times 10^{47}$ |
| | IC | $4.35^{+0.18}_{-0.31}$ | $4.63^{+2.31}_{-2.16} \times 10^{50}$ |
| Src B | PP | $2.50^{+0.10}_{-0.10}$ | $1.83^{+0.12}_{-0.10} \times 10^{45}$ |
| | IC | $3.38^{+0.16}_{-0.16}$ | $1.43^{+0.92}_{-0.59} \times 10^{49}$ |

^a The total energy of the parent protons or electrons (with energy $> 1 \text{ GeV}$) for generate the gamma-ray emission, assuming the medium density $n(\text{H})$ is $1.3 \times 10^3 \text{ cm}^{-3}$ for Src A and $4.4 \times 10^4 \text{ cm}^{-3}$ for Src B, and the distance of both Src A and Src B is 2 kpc.

with the MHD turbulence in the ISM. In this case, $D(E)$ scales as $E^{0.33 \dots 0.5}$, which predicts a softer spectrum. The difference of indices of Src A and Src B is about 0.3, which is also consistent with the index of $D(E)$ in the ISM.

In such a scenario all the gamma-ray emissions surrounding YMCs should contain two regions, in one of which the CR transport is dominated by streaming along field line and reveal a harder spectrum (inner region); in another the CR transport is dominated by scattering with MHD turbulence in the ISM (outer region). For other YMC systems, the "outer region" has not been detected yet, one reason may be that for those more powerful systems such as Cygnus cocoon, Westerlund 2, and NGC 3603, due to the larger wind power and longer age, the CR density therein is significantly higher, thus the "inner region" in which CRs transport by streaming along field lines is much larger than that in NGC 6618, and occupy the whole dense regions near the YMCs, thus dominate the produced gamma-ray emissions. In weaker systems such as W40 and W43, the "outer region" in which CR transport dominated by diffusion in MHD turbulence in ISM are too weak to be distinguished from the diffuse gamma-ray background.

In the case of "inner region", the CR streaming velocity is dominated by the balance between the damping rate and the CR streaming instability, which results a energy dependent diffusion at higher energy and predict a energy break of CR spectrum as well as the corresponding gamma-ray spectrum. As estimated in Krumholz et al. (2020) the break energy scale as $E_{\text{br}} \sim \left(\frac{\epsilon}{n^{1.5}} \right)^{\frac{1}{\gamma-1}}$, where ϵ is the CR energy density, n is the ambient gas density and γ is the spectral index of the CR (assuming a power law distribution). Thus, E_{br} can be different in different environment. Dramatically, as we mentioned above, in the case of continuous injection the CR energy density scale as $\frac{1}{r}$, which predicted a decrease of E_{br} with increasing r . For NGC 6618, such a break are not observed. But for Cygnus cocoon, a spectral softening at several TeVs have already been detected by HAWC (Abeysekara et al. 2021), if such a softening is a consequence of the propagation effects we discussed here, a spatial dependence of the energy break is expected, which may be tested by later observations.

5 CONCLUSIONS

In this work, we report the detection of gamma-ray emission toward M17 region, which hosts one of the youngest YMCs in our Galaxy, NGC 6618. In addition to Cygnus cocoon (Ackermann et al. 2011; Aharonian et al. 2019), NGC 3603 Yang & Aharonian (2017), W40 (Sun et al. 2020b), and RSGC 1 (Sun et al. 2020a), this detection provides another case in the population of gamma-ray emitting YMCs. However, the gamma-ray emission of this source has its

⁴ <http://naima.readthedocs.org/en/latest/index.html>

unique characteristic: the gamma-rays can be separated into two components, one is point-like and with harder spectrum and another is extended and with softer spectrum. Both components show spatial correlation with dense gases. Assuming the gamma-rays are produced by the interactions of CRs injected by NGC 6618 with the ambient gas, the different spectral features can be addressed by the propagation effects investigated in the environments of starburst galaxies (Krumholz et al. 2020). In this scenario, the MHD turbulent in the ISM can be damped out effectively, and CRs will stream along field lines and transport via a process of field line random walk. As a result, the CR diffusion coefficient is energy-independent at low energy and will become energy-dependent above certain break energy. The high densities of both gas and CRs in YMCs are similar to those in starburst galaxies, thus such a comparison is feasible. In M17 region, the hard spectrum of the point-like source Src B can be explained by the energy-independent diffusion. As for Src A, due to the lower gas density and CR density, the damping mechanism can be switched off, meanwhile, the diffusion coefficient are still the same as in the ISM. The features related to these propagation effects have not been observed in other YMC systems yet. But the observed energy break in Cygnus cocoon region can be explained naturally in such a scenario. Since YMCs can potentially be an alternative CR source, the propagation of CRs in the vicinity of these sources would be crucial to understand the injection of CRs to the ISM, which can be revealed by further observations with more spatial and spectral information.

6 ACKNOWLEDGEMENTS

This research made use of the data from the Milky Way Imaging Scroll Painting (MWISP) project, which is a multi-line survey in $^{12}\text{CO}/^{13}\text{CO}/\text{C}^{18}\text{O}$ along the northern galactic plane with PMO-13.7m telescope. MWISP was sponsored by National Key R&D Program of China with grant 2017YFA0402701 and CAS Key Research Program of Frontier Sciences with grant QYZDJ-SSW-SLH047. Bing Liu is supported by the NSFC under grant 12103049. Ruizhi Yang is supported by the NSFC under grants 12041305, 11421303 and the national youth thousand talents program in China. Zhiwei Chen acknowledges support from NSFC grants 11903083, 12173090, U2031202, 11873093, and 11873094.

7 DATA AVAILABILITY

The Fermi-LAT data used in this work is publicly available, which is provided online by the NASA-GSFC Fermi Science Support Center⁵. A MWISP open data proposal is required to access the CO line data used in this work, and the form could be downloaded from <http://english.dlh.pmo.cas.cn/op/odp/>.

REFERENCES

- Abdo A. A., et al., 2009, *ApJ*, **706**, L1
 Abeysekara A. U., et al., 2021, *Nature Astronomy*, **5**, 465–471
 Abramowski A., et al., 2012, *A&A*, **537**, A114
 Ackermann M., et al., 2011, *Science*, **334**, 1103
 Aharonian F. A., Atoyan A. M., 1996, *A&A*, **309**, 917
 Aharonian F., Yang R., de Oña Wilhelmi E., 2019, *Nature Astronomy*, **3**, 561

- Ballet J., Burnett T. H., Digel S. W., Lott B., 2020, arXiv e-prints, [p. arXiv:2005.11208](https://arxiv.org/abs/2005.11208)
 Cesarsky C. J., Montmerle T., 1983, *Space Sci. Rev.*, **36**, 173
 Chen Z., Jiang Z., Wang Y., Chini R., Tamura M., Nagayama T., Nagata T., Nakajima Y., 2012, *PASJ*, **64**, 110
 Chen Z., Nürnberger D. E. A., Chini R., Liu Y., Fang M., Jiang Z., 2013, *A&A*, **557**, A51
 Chen Z., Nürnberger D. E. A., Chini R., Jiang Z., Fang M., 2015, *A&A*, **578**, A82
 Chen Z., Sun W., Chini R., Haas M., Jiang Z., Chen X., 2021, *ApJ*, **922**, 90
 Chen Z., Sefako R., Yang Y., Jiang Z., Yu S., Yin J., 2022, arXiv e-prints, [p. arXiv:2204.13296](https://arxiv.org/abs/2204.13296)
 Chibueze J. O., et al., 2016, *MNRAS*, **460**, 1839
 Chini R., Elsaesser H., Neckel T., 1980, *A&A*, **91**, 186
 Domingo-Santamaría E., Torres D. F., 2006, *A&A*, **448**, 613
 Elmegreen B. G., Lada C. J., 1976, *AJ*, **81**, 1089
 Elmegreen B. G., Lada C. J., Dickinson D. F., 1979, *ApJ*, **230**, 415
 Hoffmeister V. H., Chini R., Scheyda C. M., Schulze D., Watermann R., Nürnberger D., Vogt N., 2008, *ApJ*, **686**, 310
 Jiang Z., et al., 2002, *ApJ*, **577**, 245
 Katsuta J., Uchiyama Y., Funk S., 2017, *ApJ*, **839**, 129
 Krumholz M. R., Crocker R. M., Xu S., Lazarian A., Rosevear M. T., Bedwell-Wilson J., 2020, *MNRAS*, **493**, 2817
 Lim W., De Buizer J. M., Radomski J. T., 2020, *ApJ*, **888**, 98
 Nguyen-Luong Q., et al., 2020, *ApJ*, **891**, 66
 Povich M. S., Whitney B. A., 2010, *ApJ*, **714**, L285
 Povich M. S., et al., 2009, *ApJ*, **696**, 1278
 Povich M. S., Townsley L. K., Robitaille T. P., Broos P. S., Orbin W. T., King R. R., Naylor T., Whitney B. A., 2016, *ApJ*, **825**, 125
 Ramírez-Tannus M. C., et al., 2017, *A&A*, **604**, A78
 Reid M. J., et al., 2019, *ApJ*, **885**, 131
 Saha L., Domínguez A., Tibaldo L., Marchesi S., Ajello M., Lemoine-Goumard M., López M., 2020, *ApJ*, **897**, 131
 Stutzki J., Guesten R., 1990, *ApJ*, **356**, 513
 Su Y., et al., 2019, *ApJS*, **240**, 9
 Sun X.-N., Yang R.-Z., Wang X.-Y., 2020a, *MNRAS*, **494**, 3405
 Sun X.-N., Yang R.-Z., Liang Y.-F., Peng F.-K., Zhang H.-M., Wang X.-Y., Aharonian F., 2020b, *A&A*, **639**, A80
 Wilson T. L., Hanson M. M., Muders D., 2003, *ApJ*, **590**, 895
 Xu Y., Moscadelli L., Reid M. J., Menten K. M., Zhang B., Zheng X. W., Brunthaler A., 2011, *ApJ*, **733**, 25
 Yang R.-z., Aharonian F., 2017, *A&A*, **600**, A107
 Yang R.-Z., Wang Y., 2020, *A&A*, **640**, A60
 Yang R.-z., de Oña Wilhelmi E., Aharonian F., 2018, *A&A*, **611**, A77
 Yin J., Chen Z., Yao Y., Chen J., Li B., Jiang Z., 2022, *Research in Astronomy and Astrophysics*, **22**, 035021
 Zabalza V., 2015, in 34th International Cosmic Ray Conference (ICRC2015). p. 922 ([arXiv:1509.03319](https://arxiv.org/abs/1509.03319))
 Zhan X.-L., Jiang Z.-B., Chen Z.-W., Zhang M.-M., Song C., 2016, *Research in Astronomy and Astrophysics*, **16**, 56

This paper has been typeset from a \LaTeX file prepared by the author.

⁵ <https://fermi.gsfc.nasa.gov/ssc/data/access/lat/>